Configuration comparison among kinematically optimized continuum manipulators for robotic surgeries through a single access port

Kai Xu, Jiangran Zhao and Xidian Zheng

How to cite this article:
Kai Xu, Jiangran Zhao and Xidian Zheng Configuration comparison among kinematically optimized continuum manipulators for robotic surgeries through a single access port . Robotica, Available on CJO 2014 doi:10.1017/S0263574714000976

Request Permissions : Click here

Configuration comparison among kinematically optimized continuum manipulators for robotic surgeries through a single access port

Kai Xu*, Jiangran Zhao and Xidian Zheng

RII Lab (Lab of Robotics Innovation and Intervention), UM-SJTU Joint Institute, Shanghai Jiao Tong University, Shanghai, China

SUMMARY
Many recent developments of surgical robots focus on less invasive paradigms, such as laparoscopic SPA (Single Port Access) surgery, NOTES (Natural Orifice Translumenal Endoscopic Surgery), laryngoscopic MIS (Minimally Invasive Surgery), etc. A configuration similarity shared by these surgical robots is that two or more manipulators are inserted through one access port (a laparoscope, an endoscope, or a laryngoscope) for surgical interventions. However, upon designing such a surgical robot, the structure of the inserted manipulators has not been thoroughly explored based on evaluation of their performances. This paper presents a comparison for kinematic performances among three different continuum manipulators. They all could be applied in the aforementioned surgical robots. The structural parameters of these continuum manipulators are firstly optimized to assure a more fair and consistent comparison. This study is conducted in a dimensionless manner and provides scalable results for a wide spectrum of continuum manipulator designs as long as their segments have a constant curvature. The results could serve as a design reference for future developments of surgical robots which use one access port and continuum mechanisms.

KEYWORDS: Continuum manipulator; Kinematics; Workspace; Kinematic performance; Surgical robots.

1. Introduction
MIS (Minimally Invasive Surgery), such as laparoscopy, benefits patients but hinders surgeons in their capabilities of visual perception, haptic sensing, dexterous organ manipulation, etc. In order to regain some of these encumbered capabilities, various surgical robots were constructed.[1–5] On the other hand, advances of the surgical robots and other novel tools encouraged surgeons to innovate for even less surgical invasiveness. These advances include SPA (Single Port Access) surgeries,[6] NOTES (Natural Orifice Translumenal Endoscopic Surgery) procedures,[7] and laryngoscopic MIS.[8] SPA surgery uses one skin incision (usually the umbilicus) for laparoscopic interventions, whereas NOTES procedures access the surgical site using an endoscope through the patients' natural orifices (such as vagina, GI track, etc). These new surgical paradigms use only one port to access surgical sites and perform operations. Design of a surgical robot for these new surgeries is challenging because all the system components, including a vision unit, at least two exchangeable manipulators, an illumination unit, auxiliary channels, and so on, have to be deployed through a single access port (a laparoscope, an endoscope, or a laryngoscope). In order to address the design challenges and prove feasibility, several robotic slaves were built, including the ones for SPA surgeries,[9–15] the ones for NOTES procedures,[16–21] and one for laryngoscopic MIS.[22] Two examples are shown in Fig. 1, which are the IREP robot for SPA surgeries designed by Xu *et al.*[9,11] and the NOTES surgical robot designed by Abbott *et al.*[17]
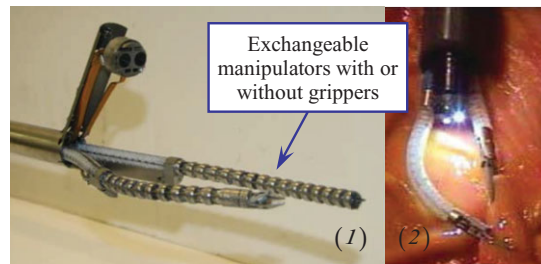
* Corresponding author: E-mail: k.xu@sjtu.edu.cn

Fig. 1. (Colour online) Surgical robotic slaves which use one access port: (1) the IREP robot for SPA surgeries,[9–11] and (2) the NOTES surgical robot.[17]

For surgical robotic slaves that use a single access port and have comparable specifications such as payload, workspace, and so on, one benchmarking parameter is the diameter of the port through which the system will be deployed. Design compactness is highly desired to achieve a smaller diameter for less invasiveness. By examining the existing designs, using properly configured continuum mechanisms might lead to a more compact design. For instance, the IREP robot for SPA surgeries which uses continuum mechanisms has 17 DoFs (Degrees of Freedom) and an outer diameter of 15mm,[9–11] whereas the continuum endoscopic surgical robot with 15 DoFs has an outer diameter of 12 mm.[21] Three facts may have contributed to the design compactness. Firstly continuum mechanisms deform themselves to transmit motions/forces and the kinematic-static compatibility between structural members is inherent. On the contrary kinematic relations in a multi-DoF rigid linkage have to be carefully planned if all the actuators will be placed proximally and this could take up extra space. Secondly preferred form closure of kinetic pairs in rigid linkages also takes additional space. What is more, components in continuum mechanisms play dual roles in structure forming and motion transmission. Besides design compactness, using continuum mechanisms introduces additional advantages such as reduced weight, compliant interaction with human anatomy, etc.

In the previous endeavors of designing compact surgical robots using continuum mechanisms,[9–11,21,22] attentions were primarily focused on satisfying the demanding geometrical constraints in order to fit everything into a small volume. Designs of the system components have not been fully optimized toward better performances. Among the required system components, the exchangeable continuum manipulators (indicated in Fig. 1) are of great importance since their kinematic and mechanical properties determine the capabilities of such a surgical robot. However, a design guide for these continuum manipulators is still missing from the existing literature.

This paper attempts to narrow this gap by presenting a kinematics study which compares the kinematic performances of three continuum manipulators with different topological structures. An investigation for improving the continuum manipulators' mechanical properties can be carried out on top of this kinematics comparison in a future study. In this study, each structure will be optimized first toward a better kinematic performance so that the comparison among them could be fair and consistent. Results of this paper could contribute to a design reference for continuum surgical robots for one-port-access procedures, such as the SPA surgeries and the NOTES procedures. A preliminary version of this paper was presented at the 2012 IEEE International Conference on Robotics and Automation (ICRA 2012).[23] In the previous conference paper, the comparison was for the three structures with their structural parameters directly from the actual implementations. The previous comparison might not be absolutely fair because the potential of each structure has not been fully explored. It's then necessary to firstly optimize each structure so that the manipulators are compared in their optimal configurations. Furthermore, all the kinematics analysis, optimizations and comparison are now performed in a dimensionless manner to provide general and scalable results for future developments of continuum surgical robots.

This paper is organized as follows. Section 2 presents the problem statement for the comparison among three different continuum manipulators. Section 3 presents the modeling nomenclature whereas Section 4 presents the kinematics of each manipulator. Optimization and dimension synthesis for each structure is presented in Section 5. The comparison results are detailed and discussed in Section 6 with conclusions followed in Section 7.
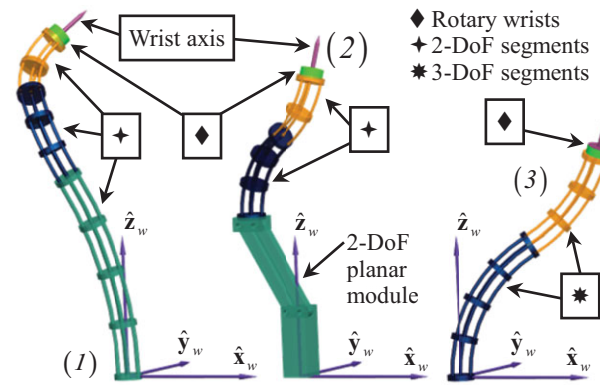
Fig. 2. (Colour online) Three 7-DoF continuum structures are compared: (1) <u>Structure A</u> consists of a 1-DoF rotary wrist and three 2-DoF segments, (2) <u>Structure B</u> consists of a 1-DoF rotary wrist, two 2-DoF segments and a 2-DoF planar translational module, and (3) <u>Structure C</u> consists of two 3-DoF segments.
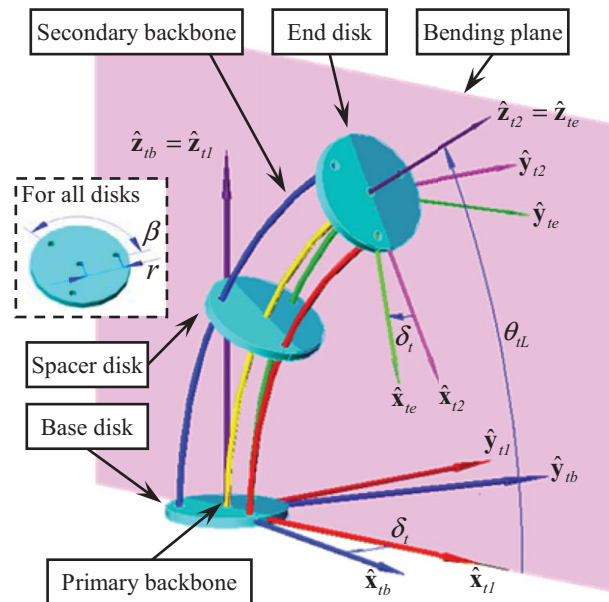

Fig. 3. (Colour online) Kinematics nomenclature of the *t*th continuum segment.

2. Comparison Formulation

In one-port-access surgeries (such as the SPA surgeries and the NOTES procedures), two or more exchangeable manipulators will be inserted through the shared access port for surgical interventions, as shown in Fig. 1. Different structures of these manipulators will lead to different system performances (e.g. workspace, distal dexterity, etc.). This paper presents a comparison for kinematic performances among continuum manipulators with three different structural topologies. The comparison results could contribute to a quantitative design reference for future developments of continuum surgical robots.

2.1. Structures of the continuum manipulators to be compared

In the surgical robots for one-port-access surgeries, the exchangeable manipulators have different numbers of DoFs: 5 DoFs,[13,21] 6 DoFs,[12] 7 DoFs,[9–11] and 8 DoFs.[22] The three kinds of continuum manipulators to be compared are shown in Fig. 2. They are extracted from the existing implementations[9–11,21,24] and they all possess 7 DoFs.

In Fig. 2, each continuum manipulator consists of two or three continuum segments (one segment is also shown in Fig. 3). Each continuum segment consists of four super-elastic backbones and

several disks, where one primary backbone is centrally located and is attached to the end disk. Three secondary backbones are equidistant from each other and from the primary backbone. The secondary backbones are attached to the end disk and can slide in holes of the base disk and the spacer disks. A 2-DoF bending motion of one continuum segment can be achieved through simultaneous pushing and pulling of the secondary backbones while keeping the length of the primary backbone constant. Length of the continuum segment is defined as the length of the primary backbone. A third DoF can be realized by actively changing the length of the primary backbone. Two or more segments can be stacked to form a manipulator with more DoFs by using concentric tubes as the backbones. The three 7-DoF structures to be compared are formed as follows, referring to Fig. 2.

- Structure A has three 2-DoF continuum segments and a 1-DoF rotary wrist. In the 2-DoF continuum segments, length of the primary backbone remains constant. This structure was applied in a palpation task using its force sensing capability.[24]
- Structure B has two 2-DoF continuum segments, a 2-DoF planar translational module, and a 1-DoF rotary wrist. This structure was applied in the IREP robot for SPA surgeries.[9–11]
- Structure C has two 3-DoF continuum segments and a 1-DoF rotary wrist. The third DoF of the continuum segment is realized by actively changing the length of the primary backbone. This structure was intended for an endoscopic surgical robot for NOTES procedures.[21]

In this study, grippers are not considered since the choices for grippers vary a lot for different procedures. Generality and applicability of this study will hold as long as the size of a selected gripper can be considered small with respect to the overall size of the continuum manipulator.

To be noted, although the structures to be compared all have continuum segments that are formed using multiple elastic backbones, these segments can be replaced by other designs as far as they can be described by the kinematics presented in Section 4. Examples of the applicable designs might include the ones.[25–28]

2.2. Evaluation of the kinematic performance

The kinematic performance of a manipulator could be described by its workspace and manipulability. The workspace includes both the translational workspace and the orientation workspace (the dexterous workspace). Measures of the manipulability were intensively studied[29–31] and most measures involve different interpretation of the singular values of the manipulator's Jacobian matrix with or without normalization, such as determinant, condition number, etc.

A Jacobian matrix represents the mapping between the velocities (or the general actuation forces) in a manipulator's joint space and the Euclidian velocities (or the wrenches) of the end effector. Unlike industrial robotic applications in which speed, precision, stiffness, and so on are emphasized for higher productivity and efficiency, surgical robots are designed towards different considerations such as safety, compactness, compliance, and delicacy. Within a translational workspace which envelopes the targeted surgical site, surgeons are more concerned about whether they can orient a tool and approach an organ as desired. Speed of surgical manipulation is usually concerned secondarily and the manipulation speed can be relatively easily improved by using more powerful actuators.

The paper proposes to evaluate the kinematic performance of each continuum manipulator as the solid angles swept by the wrist axis of the manipulator at the selected points, as shown in Figs. 10–12. A similar practice can be found from an existing study.[32] These selected points are the vertices and the central point of a cubic functional volume fitted in each manipulator's translational workspace. When the translational workspace envelops the same functional volume, the solid angle swept indicates how freely the surgical end effectors can be oriented. The orientation (the roll angle) about the wrist axis can always be achieved due to the presence of the distal rotary wrist. This evaluation formulation is simply referred to as the evaluation of the kinematic performance, avoiding the possible back-and-forth discussion of defining a specific term, such as distal dexterity.

In order to make the comparison fair and consistent, all the manipulators will have the same reach (the furthest reachable point along $\hat{\mathbf{z}}_w$ in Fig. 2). Their structural parameters will be firstly optimized as in Section 5. Unlike the design optimizations performed for serial and parallel robots,[33] the optimization in Section 5 is performed in an enumerative manner due to the specific formulation of the optimization and the kinematics of continuum robots. During the optimization, the scope of this comparison will be slightly expanded to include Structure B1, B2, C1, and C2. Structure B1 and B2 are topologically similar but with different dimensions, so are Structure C1 and C2. Section 5

Table I. Nomenclature used in this paper.*.

i	Index of the secondary backbones, $i = 1, 2, 3$
t	Index of the segments, $t = 1, 2, \ldots, n$; numbering of the segments always precedes the secondary backbones.
r	Radius of the pitch circle defining the positions of the secondary backbones in all the disks.
β	Division angle of the secondary backbones along the circumference of the pitch circle, $\beta = 2\pi/3$.
L_t, L_{ti}	Length of the primary and the ith secondary backbone of the tth segment
ρ_t	Bending radius of the primary backbone of the tth segment
$\mathbf{q}_t$	$\mathbf{q}_t = [\, q_{t1} \; q_{t2} \; q_{t3} \,]^T$ is the actuation length vector in the joint space of the tth segment, where $q_{ti} \equiv L_{ti} - L_t$.
$\theta_t (s)$	The angle of the tangent to the primary backbone in the bending plane of the tth segment. $\theta_t (L_t)$ and $\theta_t (0)$ are designated by θ_{tL} and θ_0. $\theta_0 = \pi/2$ is a constant.
δ_{ti}	For the tth segment, a right-handed rotation angle from $\hat{\mathbf{x}}_{t1}$ about $\hat{\mathbf{z}}_{t1}$ to a line passing through the primary backbone and the ith secondary backbone. At a straight configuration $\hat{\mathbf{x}}_{t1}$ is along the same direction as the desired instantaneous linear velocity of the end disk.
δ_t	$\delta_t \equiv \delta_{t1}$ and $\delta_{ti} = \delta_t + (i - 1)\,\beta, i = 1, 2, 3$
$\boldsymbol{\psi}_t$	$\boldsymbol{\psi}_t = [\, \theta_{tL} \; \delta_t \,]^T$ is a configuration vector to define the pose of the tth segment.
$\mathbf{J}_{t\,\mathbf{x}\boldsymbol{\psi}}$	$\dot{\mathbf{x}}_t = \mathbf{J}_{t\,\mathbf{x}\boldsymbol{\psi}}\,\dot{\boldsymbol{\psi}}_t$ where $\dot{\mathbf{x}}_t$ (the linear velocity precedes the angular velocity) is the twist of the end disk of the tth segment in $\{tb\}$.
$\mathbf{J}_{t\,\mathbf{q}\boldsymbol{\psi}}$	Jacobian matrix of the mapping $\dot{\mathbf{q}}_t = \mathbf{J}_{t\,\mathbf{q}\boldsymbol{\psi}}\,\dot{\boldsymbol{\psi}}_t$
$^1\mathbf{R}_2$	Coordinate transformation matrix from frame *2* to frame *1*.
$^{tb}\mathbf{p}_t (s)$	Position vector of a point along the primary backbone of the tth segment described in $\{tb\}$ and $^{tb}\mathbf{p}_{tL} \equiv {}^{tb}\mathbf{p}_t (s = L_t)$.

* The table is also 80 mm wide.

elaborates how these derivative structures are generated. The inclusion of more structures in this comparison could potentially better assist designers when they make type synthesis decisions.

This study only concerns the kinematic performance of one manipulator since the two manipulators will be deployed through the same access port. The offset between them can be considered small and their translational workspaces largely overlap. The kinematic performance of one manipulator hence normally indicates that of a dual-arm surgical robot.

3. Model Nomenclature
All three structures in Fig. 2 use multiple continuum segments. Since these segments are structurally similar, Fig. 3 only shows the tth segment ($t = 1, 2,$ or 3). Nomenclatures are defined in Table I, while coordinate systems of the tth segment are defined as below:

- *Base Disk Coordinate System* (BDS) of the tth segment $\{tb\} \equiv \{\hat{\mathbf{x}}_{tb}, \hat{\mathbf{y}}_{tb}, \hat{\mathbf{z}}_{tb}\}$ is attached to the base disk of the tth segment, whose XY plane coincides with the base disk and its origin is at the center of the base disk. $\hat{\mathbf{x}}_{tb}$ points from the center of the base disk to the first secondary backbone while $\hat{\mathbf{z}}_{tb}$ is perpendicular to the base disk. The secondary backbones are numbered according to the definition of δ_{ti}.
- *Bending Plane Coordinate System 1* (BPS1) of the tth segment $\{t1\} \equiv \{\hat{\mathbf{x}}_{t1}, \hat{\mathbf{y}}_{t1}, \hat{\mathbf{z}}_{t1}\}$ shares its origin with $\{tb\}$, while the continuum segment bends in its XZ plane.
- *Bending Plane Coordinate System 2* (BPS2) of the tth segment $\{t2\} \equiv \{\hat{\mathbf{x}}_{t2}, \hat{\mathbf{y}}_{t2}, \hat{\mathbf{z}}_{t2}\}$ is obtained from $\{t1\}$ by a rotation about $\hat{\mathbf{y}}_{t1}$ such that $\hat{\mathbf{z}}_{t1}$ becomes backbone tangent at the end disk. Origin of $\{t2\}$ is at center of the end disk.
- *End Disk Coordinate System* (EDS) of the tth segment $\{te\} \equiv \{\hat{\mathbf{x}}_{te}, \hat{\mathbf{y}}_{te}, \hat{\mathbf{z}}_{te}\}$ is fixed to the end disk. $\hat{\mathbf{x}}_{te}$ points from center of the end disk to the first secondary backbone and $\hat{\mathbf{z}}_{te}$ is normal to the end disk. $\{te\}$ is obtained from $\{t2\}$ by a rotation about $\hat{\mathbf{z}}_{t2}$.

When multiple segments are stacked, these segments are numbered from the most proximal one, as indicated in Figs. 4 and 5. Between the tth and $(t+1)$th segments, $\{te\}$ coincides with $\{(t+1)b\}$. In other words, $^{te}\mathbf{R}_{(t+1)b}$ is an identity matrix or $^{tb}\mathbf{R}_{(t+1)b} = {}^{tb}\mathbf{R}_{te}{}^{te}\mathbf{R}_{(t+1)b} = {}^{tb}\mathbf{R}_{te}$, while $^{tb}\mathbf{R}_{te}$ is as in Eq. (3).
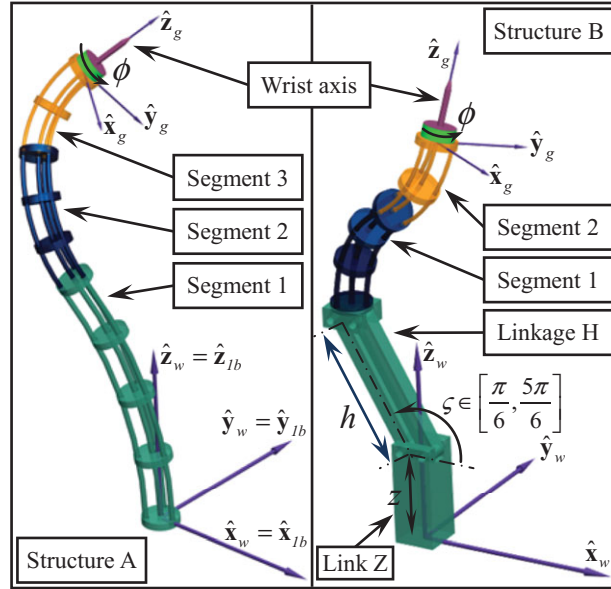
Fig. 4. (Colour online) Structure A and Structure B with the configuration vectors defined as $\boldsymbol{\xi}_A = [\phi \ \boldsymbol{\psi}_3^T \ \boldsymbol{\psi}_2^T \ \boldsymbol{\psi}_1^T]^T$ and $\boldsymbol{\xi}_B = [\phi \ \boldsymbol{\psi}_2^T \ \boldsymbol{\psi}_1^T \ \varsigma \ z]^T$, respectively.
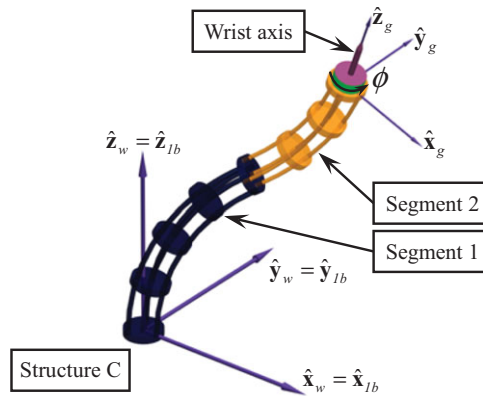
Fig. 5. (Colour online) Structure C with its configuration vector $\boldsymbol{\xi}_C = [\phi \ \boldsymbol{\psi}_2^T \ L_2 \ \boldsymbol{\psi}_1^T \ L_1]^T$.

4. Kinematics

Thorough analysis of one continuum segment's kinematics[22,24,34−36] is developed from early work.[37−39] Related entities are summarized here for completeness. Kinematics of one segment will be used to assemble the kinematics of the three continuum manipulators.

4.1. Kinematics of the tth segment

Kinematics expressions of the tth segment are based on an assumption that curvature along the primary backbone is constant. This assumption was verified by the experiments[24,40] for the multi-backbone continuum segment shown in Fig. 3, and also by the experiments[27,41,42] for a variety of different designs.

$\boldsymbol{\psi}_t = [\theta_{tL} \ \delta_t]^T$ parameterizes the tth continuum segment. Related kinematics expressions are summarized as follows with the symbol definitions listed in Table I. Derivations are detailed in a previous publication.[24]

$$L_{ti} = L_t + q_{ti} = L_t + r \cos(\delta_{ti})(\theta_{tL} - \theta_0), \quad i = 1, 2, 3 \tag{1}$$

$$ {}^{tb}\mathbf{p}_{tL} = \frac{L_t}{\theta_{tL} - \theta_0} \begin{bmatrix} \cos\delta_t \, (\sin\theta_{tL} - 1) \\ \sin\delta_t \, (1 - \sin\theta_{tL}) \\ -\cos\theta_{tL} \end{bmatrix} \tag{2} $$

where ${}^{tb}\mathbf{p}_{tL} = [\,0\ 0\ L_t\,]^T$ when $\theta_{tL} \to \theta_0 = \pi/2$. Transformation matrix ${}^{tb}\mathbf{R}_{te}$ relates $\{te\}$ to $\{tb\}$:

$$ {}^{tb}\mathbf{R}_{te} = R\,(\hat{\mathbf{z}}_{tb}, -\delta_t)\, R\,(\hat{\mathbf{y}}_{t1}, \theta_0 - \theta_{tL})\, R\,(\hat{\mathbf{z}}_{t2}, \delta_t) \tag{3} $$

where $R(\hat{\mathbf{n}}, \gamma)$ designates a rotation about $\hat{\mathbf{n}}$ by γ.

The instantaneous kinematics is given by:

$$ \dot{\mathbf{x}}_t = \mathbf{J}_{t\,\mathbf{x}\boldsymbol{\psi}}\, \dot{\boldsymbol{\psi}}_t, \quad \text{where} \quad \mathbf{J}_{t\mathbf{x}\boldsymbol{\psi}} = \begin{bmatrix} \mathbf{J}_{t\mathbf{v}} \\ \mathbf{J}_{t\boldsymbol{\omega}} \end{bmatrix}, \tag{4} $$

$$ \mathbf{J}_{t\mathbf{v}} = \begin{bmatrix} L_t \cos\delta_t \dfrac{(\theta_{tL} - \theta_0)\cos\theta_{tL} - \sin\theta_{tL} + 1}{(\theta_{tL} - \theta_0)^2} & -L_t \dfrac{\sin\delta_t(\sin\theta_{tL} - 1)}{\theta_{tL} - \theta_0} \\[3mm] -L_t \sin\delta_t \dfrac{(\theta_{tL} - \theta_0)\cos\theta_{tL} - \sin\theta_{tL} + 1}{(\theta_{tL} - \theta_0)^2} & -L_t \dfrac{\cos\delta_t(\sin\theta_{tL} - 1)}{\theta_{tL} - \theta_0} \\[3mm] L_t \dfrac{(\theta_{tL} - \theta_0)\sin\theta_{tL} + \cos\theta_{tL}}{(\theta_{tL} - \theta_0)^2} & 0 \end{bmatrix}, $$

$$ \mathbf{J}_{t\boldsymbol{\omega}} = \begin{bmatrix} -\sin\delta_t & \cos\delta_t \cos\theta_{tL} \\ -\cos\delta_t & -\sin\delta_t \cos\theta_{tL} \\ 0 & -1 + \sin\theta_{tL} \end{bmatrix}. \tag{5} $$

Singularity of $\mathbf{J}_{t\mathbf{x}\boldsymbol{\psi}}$ for $\theta_{tL} \to \theta_0 = \pi/2$ can be resolved by applying L'Hopital rule.

$$ \lim_{\theta_{tL} \to \theta_0 = \frac{\pi}{2}} \mathbf{J}_{t\mathbf{x}\boldsymbol{\psi}} = \begin{bmatrix} -L_t \cos\delta_t/2 & 0 \\ L_t \sin\delta_t/2 & 0 \\ 0 & 0 \\ -\sin\delta_t & 0 \\ -\cos\delta_t & 0 \\ 0 & 0 \end{bmatrix}. \tag{6} $$

4.2. Kinematics of Structure A

A manipulator which uses <u>Structure A</u> was tested for its force sensing capability,[24] as shown in Fig. 4. In the world coordinate system $\{w\} = \{1b\}$, <u>Structure A</u> consists of the following components, referring to Fig. 4.

- Continuum segment 1 with coordinate systems from $\{w\} = \{1b\}$ to $\{1e\}$ attached, referring to Fig. 3.
- Continuum segment 2 is stacked on top of the segment 1 with coordinate systems from $\{2b\}$ to $\{2e\}$ attached. $\{2b\}$ coincides with $\{1e\}$, or ${}^{1b}\mathbf{R}_{2b} = {}^{1b}\mathbf{R}_{1e}$.
- Continuum segment 3 is stacked on top of the segment 2 with coordinate systems from $\{3b\}$ to $\{3e\}$ attached. $\{3b\}$ coincides with $\{2e\}$, or ${}^{2b}\mathbf{R}_{3b} = {}^{2b}\mathbf{R}_{2e}$.
- A wrist with a coordinate system $\{g\} \equiv \{\hat{\mathbf{x}}_g, \hat{\mathbf{y}}_g, \hat{\mathbf{z}}_g\}$ attached. $\{g\}$ is obtained from $\{3e\}$ by a rotation of ϕ about $\hat{\mathbf{z}}_g = \hat{\mathbf{z}}_{3e}$. When a specific gripper is attached to the wrist, the gripper can rotate with respect to the wrist and its shape can be defined in $\{g\}$; e.g., tip of a gripper in $\{g\}$ can be characterized by ${}^g\mathbf{p}_g$. Since a gripper is not considered in this study, ${}^g\mathbf{p}_g = \mathbf{0}$.

A configuration vector $\boldsymbol{\xi}_A = [\,\phi\ \boldsymbol{\psi}_3^T\ \boldsymbol{\psi}_2^T\ \boldsymbol{\psi}_1^T\,]^T$ can be defined for the parameterization of Structure A. In order to provide a general representation, tip position ${}^w\mathbf{p}_g$ and Jacobian of the gripper with

respect to $\{w\} = \{1b\}$ can be derived as follows. If a gripper is not considered, ${}^g\mathbf{p}_g$ can be simply set as $\mathbf{0}$.

$$
{}^w\mathbf{p}_g = {}^{1b}\mathbf{p}_{1L} + {}^{1b}\mathbf{R}_{2b}\left({}^{2b}\mathbf{p}_{2L} + {}^{2b}\mathbf{R}_{3b}\left({}^{3b}\mathbf{p}_{3L} + {}^{3b}\mathbf{R}_g{}^g\mathbf{p}_g\right)\right), \tag{7}
$$

where ${}^{3b}\mathbf{R}_g = {}^{3b}\mathbf{R}_{3e}{}^{3e}\mathbf{R}_g$; ${}^{1b}\mathbf{p}_{1L}$, ${}^{2b}\mathbf{p}_{2L}$ and ${}^{3b}\mathbf{p}_{3L}$ are from Eq. (2),

$$
{}^w\dot{\mathbf{x}} = \mathbf{J}_A\dot{\boldsymbol{\xi}}_A, \tag{8}
$$

$$
\mathbf{J}_A = \begin{bmatrix} \mathbf{0}_{3\times 1} & {}^{1b}\mathbf{R}_{3b}\mathbf{T}_{A3} & {}^{1b}\mathbf{R}_{2b}\mathbf{T}_{A2} & \mathbf{T}_{A1} \\ {}^{1b}\mathbf{R}_{3b}{}^{3b}\mathbf{R}_g\hat{\mathbf{z}}_g & {}^{1b}\mathbf{R}_{3b}\mathbf{J}_{3\boldsymbol{\omega}} & {}^{1b}\mathbf{R}_{2b}\mathbf{J}_{2\boldsymbol{\omega}} & \mathbf{J}_{1\boldsymbol{\omega}} \end{bmatrix}, \tag{9}
$$

where ${}^{1b}\mathbf{R}_{3b} = {}^{1b}\mathbf{R}_{2b}{}^{2b}\mathbf{R}_{3b}$, ${}^{3b}\mathbf{R}_g = {}^{3b}\mathbf{R}_{3e}{}^{3e}\mathbf{R}_g$ and ${}^{1b}\mathbf{R}_g = {}^{1b}\mathbf{R}_{3b}{}^{3b}\mathbf{R}_g$; $\mathbf{T}_{A3}$, $\mathbf{T}_{A2}$, and $\mathbf{T}_{A1}$ are written as below:

$$
\mathbf{T}_{A3} = \mathbf{J}_{3\mathbf{v}} - \left[{}^{3b}\mathbf{R}_g{}^g\mathbf{p}_g\right]^{\times}\mathbf{J}_{3\boldsymbol{\omega}}, \tag{10}
$$

$$
\mathbf{T}_{A2} = \mathbf{J}_{2\mathbf{v}} - \left[{}^{2b}\mathbf{R}_{3b}{}^{3b}\mathbf{p}_{3L} + {}^{2b}\mathbf{R}_{3b}{}^{3b}\mathbf{R}_g{}^g\mathbf{p}_g\right]^{\times}\mathbf{J}_{2\boldsymbol{\omega}}, \tag{11}
$$

$$
\mathbf{T}_{A1} = \mathbf{J}_{1\mathbf{v}} - \left[{}^{1b}\mathbf{R}_{2b}{}^{2b}\mathbf{p}_{2L} + {}^{1b}\mathbf{R}_{3b}{}^{3b}\mathbf{p}_{3L} + {}^{1b}\mathbf{R}_g{}^g\mathbf{p}_g\right]^{\times}\mathbf{J}_{1\boldsymbol{\omega}}, \tag{12}
$$

where $[\mathbf{p}]^{\times}$ is the skew-symmetric matrix of a vector $\mathbf{p}$; $\mathbf{J}_{1\mathbf{v}}$, $\mathbf{J}_{1\boldsymbol{\omega}}$, $\mathbf{J}_{2\mathbf{v}}$, $\mathbf{J}_{2\boldsymbol{\omega}}$, $\mathbf{J}_{3\mathbf{v}}$, and $\mathbf{J}_{3\boldsymbol{\omega}}$ are from Eq. (5). $\mathbf{J}_A$ would be used later in a pseudo-inverse formulation to drive Structure A for evaluation of the kinematic performance.

4.3. Kinematics of Structure B
Continuum manipulators which use <u>Structure B</u> were adopted in the IREP robot for SPA surgeries,[9–11] as shown in Fig. 4. In the world coordinate system $\{w\} \equiv \{\hat{\mathbf{x}}_w, \hat{\mathbf{y}}_w, \hat{\mathbf{z}}_w\}$, <u>Structure B</u> consists of the following components.

- Link Z which provides a translation z along $\hat{\mathbf{z}}_w$.
- Linkage H has a parallelogram form and sits on top of Link Z. It opens to an angle of ς and translates $\{1b\}$ for a distance of h.
- Continuum segment 1 with coordinate systems from $\{1b\}$ to $\{1e\}$ attached. $\{1b\}$ is parallel to $\{w\}$.
- Continuum segment 2 is stacked on top of the segment 1 with coordinate systems from $\{2b\}$ to $\{2e\}$ attached. $\{2b\}$ coincides with $\{1e\}$, or ${}^{1b}\mathbf{R}_{2b} = {}^{1b}\mathbf{R}_{1e}$.
- A wrist with a coordinate system $\{g\} \equiv \{\hat{\mathbf{x}}_g, \hat{\mathbf{y}}_g, \hat{\mathbf{z}}_g\}$ attached. $\{g\}$ is obtained from $\{2e\}$ by a rotation of ϕ. If a gripper is attached to the wrist, the gripper tip in $\{g\}$ is defined as ${}^g\mathbf{p}_g$. If the gripper is neglected, ${}^g\mathbf{p}_g = \mathbf{0}$.

Actual realization of this structure was detailed in a previous publication.[9] A configuration vector $\boldsymbol{\xi}_B = [\phi \ \boldsymbol{\psi}_2^T \ \boldsymbol{\psi}_1^T \ \varsigma \ z]^T$ can be defined for kinematics parameterization. Tip position and Jacobian of the gripper in $\{w\}$ can be derived as the following. Detailed derivations were published.[10,11]

$$
{}^w\mathbf{p}_g = {}^w\mathbf{p}_{1b} + {}^{1b}\mathbf{p}_{1L} + {}^{1b}\mathbf{R}_{1e}\left({}^{2b}\mathbf{p}_{2L} + {}^{2b}\mathbf{R}_g{}^g\mathbf{p}_g\right), \tag{13}
$$

where ${}^w\mathbf{p}_{1b} = z\hat{\mathbf{z}}_w + h\cos\varsigma\hat{\mathbf{x}}_w + h\sin\varsigma\hat{\mathbf{z}}_w$ and ${}^{2b}\mathbf{R}_g = {}^{2b}\mathbf{R}_{2e}{}^{2e}\mathbf{R}_g$. ${}^{1b}\mathbf{p}_{1L}$ and ${}^{2b}\mathbf{p}_{2L}$ are from Eq. (2).

$$
{}^w\dot{\mathbf{x}} = \mathbf{J}_B\dot{\boldsymbol{\xi}}_B, \tag{14}
$$

$$
\mathbf{J}_B = \begin{bmatrix} \mathbf{0}_{3\times 1} & {}^{1b}\mathbf{R}_{2b}\mathbf{T}_{B2} & \mathbf{T}_{B1} & \mathbf{t}_B & \hat{\mathbf{z}}_w \\ {}^{1b}\mathbf{R}_g\hat{\mathbf{z}}_g & {}^{1b}\mathbf{R}_{2b}\mathbf{J}_{2\boldsymbol{\omega}} & \mathbf{J}_{1\boldsymbol{\omega}} & \mathbf{0}_{3\times 1} & \mathbf{0}_{3\times 1} \end{bmatrix}. \tag{15}
$$

where $^{1b}\mathbf{R}_g = {}^{1b}\mathbf{R}_{2b}{}^{2b}\mathbf{R}_g$. $\mathbf{T}_{B2}$, $\mathbf{T}_{B1}$, and $\mathbf{t}_B$ are written as follows:

$$\mathbf{T}_{B2} = \mathbf{J}_{2\mathbf{v}} - \left[{}^{2b}\mathbf{R}_g{}^g\mathbf{p}_g\right]^\times \mathbf{J}_{2\boldsymbol{\omega}} \tag{16}$$

$$\mathbf{T}_{B1} = \mathbf{J}_{1\mathbf{v}} - \left[{}^{1b}\mathbf{R}_{2b}{}^{2b}\mathbf{p}_{2L} + {}^{1b}\mathbf{R}_g{}^g\mathbf{p}_g\right]^\times \mathbf{J}_{1\boldsymbol{\omega}} \tag{17}$$

$$\mathbf{t}_B = \frac{\partial}{\partial \varsigma}\left({}^w\mathbf{p}_{1b}\right) = -h\sin\varsigma\,\hat{\mathbf{x}}_w + h\cos\varsigma\,\hat{\mathbf{z}}_w \tag{18}$$

where $\mathbf{J}_{1\mathbf{v}}, \mathbf{J}_{1\boldsymbol{\omega}}, \mathbf{J}_{2\mathbf{v}}$, and $\mathbf{J}_{2\boldsymbol{\omega}}$ are from Eq. (5). $\mathbf{J}_B$ would be used later in a pseudo-inverse formulation to drive Structure B for evaluation of the kinematic performance.

4.4. Kinematics of Structure C
Structure C was intended for an endoscopic surgical robot for NOTES procedures.[21] The actual implementation is slightly different from the kinematic schematic as in Fig. 5 due to geometrical and mechanical considerations. In the world coordinate system $\{w\} = \{1b\}$, Structure C consists of the following components.

- Continuum segments 1 and 2 are stacked with coordinate systems from $\{1b\}$ to $\{1e\}$ and $\{2b\}$ to $\{2e\}$ attached. $\{2b\}$ coincides with $\{1e\}$, or $^{1b}\mathbf{R}_{2b} = {}^{1b}\mathbf{R}_{1e}$. Length of each segment (L_1 and L_2) now can be actively controlled to introduce an additional DoF.
- A wrist with a coordinate system $\{g\} \equiv \left\{\hat{\mathbf{x}}_g, \hat{\mathbf{y}}_g, \hat{\mathbf{z}}_g\right\}$ attached. $\{g\}$ is obtained from $\{2e\}$ by a rotation of ϕ. If a gripper is attached to the wrist, the gripper tip in $\{g\}$ is defined as $^g\mathbf{p}_g$. If the gripper is neglected, $^g\mathbf{p}_g = \mathbf{0}$.

A configuration vector $\boldsymbol{\xi}_C = \begin{bmatrix} \phi & \boldsymbol{\psi}_2^T & L_2 & \boldsymbol{\psi}_1^T & L_1 \end{bmatrix}^T$ can be defined for the parameterization. Tip position of the gripper in $\{w\}$ can be written as the following:

$$^w\mathbf{p}_g = {}^{1b}\mathbf{p}_{1L} + {}^{1b}\mathbf{R}_{2b}\left({}^{2b}\mathbf{p}_{2L} + {}^{2b}\mathbf{R}_{2e}{}^{2e}\mathbf{R}_g{}^g\mathbf{p}_g\right), \tag{19}$$

where $^{1b}\mathbf{p}_{1L}$ and $^{2b}\mathbf{p}_{2L}$ are from Eq. (2).

Jacobian matrix can be derived by writing linear velocity and angular velocity of the gripper as follows:

$$^w\mathbf{v}_g = \mathbf{J}_{1\mathbf{v}}\dot{\boldsymbol{\psi}}_1 + \mathbf{J}_{1\boldsymbol{\omega}}\dot{\boldsymbol{\psi}}_1 \times \left({}^{1b}\mathbf{R}_{2b}{}^{2b}\mathbf{p}_{2L} + {}^{1b}\mathbf{R}_g{}^g\mathbf{p}_g\right) + \frac{\partial\left({}^{1b}\mathbf{p}_{1L}\right)}{\partial L_1}$$
$$+ {}^{1b}\mathbf{R}_{2b}\left(\mathbf{J}_{2\mathbf{v}}\dot{\boldsymbol{\psi}}_2 + \mathbf{J}_{2\boldsymbol{\omega}}\dot{\boldsymbol{\psi}}_2 \times \left({}^{2b}\mathbf{R}_g{}^g\mathbf{p}_g\right) + \frac{\partial\left({}^{2b}\mathbf{p}_{2L}\right)}{\partial L_2}\right), \tag{20}$$

where $^{1b}\mathbf{R}_g = {}^{1b}\mathbf{R}_{2b}{}^{2b}\mathbf{R}_{2e}{}^{2e}\mathbf{R}_g$ and $^{2b}\mathbf{R}_g = {}^{2b}\mathbf{R}_{2e}{}^{2e}\mathbf{R}_g$.

$$^w\boldsymbol{\omega}_g = \mathbf{J}_{1\boldsymbol{\omega}}\dot{\boldsymbol{\psi}}_1 + {}^{1b}\mathbf{R}_{2b}\mathbf{J}_{2\boldsymbol{\omega}}\dot{\boldsymbol{\psi}}_2 + \dot{\phi}{}^{1b}\mathbf{R}_g\hat{\mathbf{z}}_g \tag{21}$$

Then, the Jacobian can be written as follows:

$$^w\dot{\mathbf{x}} = \mathbf{J}_C\dot{\boldsymbol{\xi}}_C, \tag{22}$$

$$\mathbf{J}_C = \begin{bmatrix} \mathbf{0}_{3\times 1} & {}^{1b}\mathbf{R}_{2b}\mathbf{T}_{C2} & {}^{1b}\mathbf{R}_{2b}\mathbf{t}_{C2} & \mathbf{T}_{C1} & \mathbf{t}_{C1} \\ {}^{1b}\mathbf{R}_g\hat{\mathbf{z}}_g & {}^{1b}\mathbf{R}_{2b}\mathbf{J}_{2\boldsymbol{\omega}} & \mathbf{0}_{3\times 1} & \mathbf{J}_{1\boldsymbol{\omega}} & \mathbf{0}_{3\times 1} \end{bmatrix}, \tag{23}$$

where $\mathbf{T}_{C2}$, $\mathbf{t}_{C2}$, $\mathbf{T}_{C1}$, and $\mathbf{t}_{C1}$ are written as follows:

$$\mathbf{T}_{C2} = \mathbf{J}_{2\mathbf{v}} - \left[{}^{2b}\mathbf{R}_g{}^g\mathbf{p}_g\right]^\times \mathbf{J}_{2\boldsymbol{\omega}}, \tag{24}$$

$$\mathbf{t}_{Ct} = \frac{[\cos\delta_t(\sin\theta_{tL}-1) \quad \sin\delta_t(1-\sin\theta_{tL}) \quad -\cos\theta_{tL}]^T}{\theta_{tL}-\theta_0}. \tag{25}$$

For $\mathbf{t}_{C2}$ and $\mathbf{t}_{C1}$, $\mathbf{t}_{Ct}=[\,0\;0\;1\,]^T$ when $\theta_{tL}\to\theta_0=\pi/2$.

$$\mathbf{T}_{C1}=\mathbf{J}_{1\mathbf{v}}-\left[{}^{1b}\mathbf{R}_{2b}{}^{2b}\mathbf{p}_{2L}+{}^{1b}\mathbf{R}_g{}^g\mathbf{p}_g\right]^\times\mathbf{J}_{1\boldsymbol{\omega}}, \tag{26}$$

where $\mathbf{J}_{1\mathbf{v}}$, $\mathbf{J}_{1\boldsymbol{\omega}}$, $\mathbf{J}_{2\mathbf{v}}$, and $\mathbf{J}_{2\boldsymbol{\omega}}$ are from Eq. (5). $\mathbf{J}_C$ would be used later in a pseudo-inverse formulation to drive Structure C for the kinematic performance evaluation.

5. Kinematic Optimization of the Continuum Manipulators
This paper presents a comparison that could be used as a quantitative design reference for future developments of continuum surgical robots using one-port access. The comparison should examine these structures at their optimal configurations so that the comparison is fair and consistent.

This section will first optimize Structure A for its optimal kinematic performance. As shown later, since the theoretical optimum could not be realized by a physical design, the optimization is then relaxed to a realistic configuration of Structure A, taking practical constraints into consideration. The configurations of Structure B and Structure C are then optimized with respect to the same constraints so that a more consistent comparison for kinematic performances could be presented in Section 6.

To be noted, a predetermined constraint adopted in this study is that each continuum segment could only undergo a 90° bending, namely, $\theta_{tL}\in[0,\pi/2]$. The reason is mainly that the published experimental validations of the constant-curvature assumption were mostly up to 90° in bending. Validity of extending this assumption beyond the 90° bending is not guaranteed.

This study is conducted in a dimensionless manner and reach of each structure is assumed to be 1 (reach is defined as the furthest reachable point along $\hat{\mathbf{z}}_w$ in Fig. 2). Results of this paper can be easily scaled for a practical case.

The selection of a gripper is usually procedure-dependent and different grippers could lead to different results of the optimizations and the comparison. A gripper is excluded from this study for better consistence in the optimizations and the comparison. Generality and applicability of this study shall be preserved as long as size of a selected gripper can be considered small with respect to the overall size of the manipulator. Although the kinematics in Section 4 does include a gripper for derivation completeness, it is easy to set ${}^g\mathbf{p}_g=\mathbf{0}$ for the absence of a gripper.

According to Section 2.2, the kinematic performance is evaluated as the capability how these continuum manipulators can orient surgical tools at the vertices and the center of a cubic functional volume. It can be seen from Section 6 that the evaluation of the proposed kinematic performance is not an analytic process. Although a general method for robot workspace determination has been introduced recently for articulated robots,[43] no such general methods exist for continuum manipulators. Directly formulating optimizations of the three continuum manipulators towards better kinematic performances can be formidable.

Instead of directly optimizing the manipulators for better kinematic performances, optimizations were alternatively conducted to maximize the margin between the functional volume and the boundary of the manipulators' translational workspace. The reason is explained as follows. Generally, a manipulator's orientation workspace could have nothing to do with its translational workspace. However, regarding a manipulator that uses these continuum segments, the translational workspace usually has an outer boundary and an inner boundary as shown in Figs. 6, 8, and 9. Points on the outer boundary could be reached only when one or more segments are straight ($\theta_{tL}=\pi/2$). At the mean time points on the inner boundary could be reached only when one or more segments are maximally bent ($\theta_{tL}=0$). The orientation workspace heavily depends on the available bending ranges of these continuum segments. When a point is close to the boundary of the translational workspace, one or more segments are bounded to zero or maximal bending, which would lead to a worse kinematic performance. With a bigger margin, vertices of the functional volume can be placed further away from the boundary, which is expected to introduce a better kinematic performance whose definition is proposed in Section 2.2. This approach is echoed by the comparison results in Section 6. It should
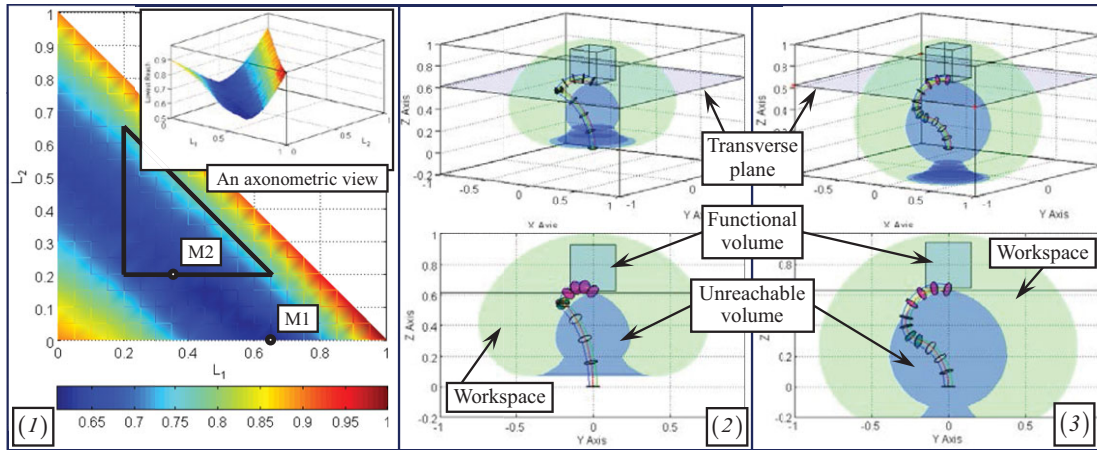
Fig. 6. (Colour online) Optimization of Structure A: (1) The lowest reach under various configurations, (2) the theoretical optimal configuration ($L_1 = 0.65$, $L_2 = 0.0$, and $L_3 = 0.35$), and (3) the feasible optimal configuration ($L_1 = 0.35$, $L_2 = 0.20$, and $L_3 = 0.45$).
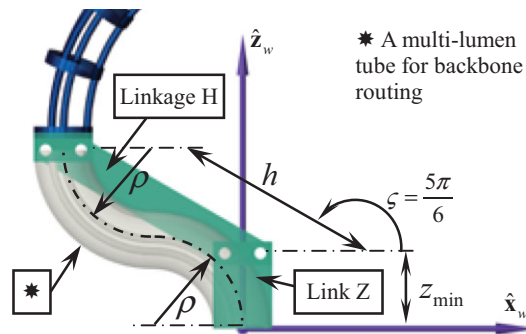

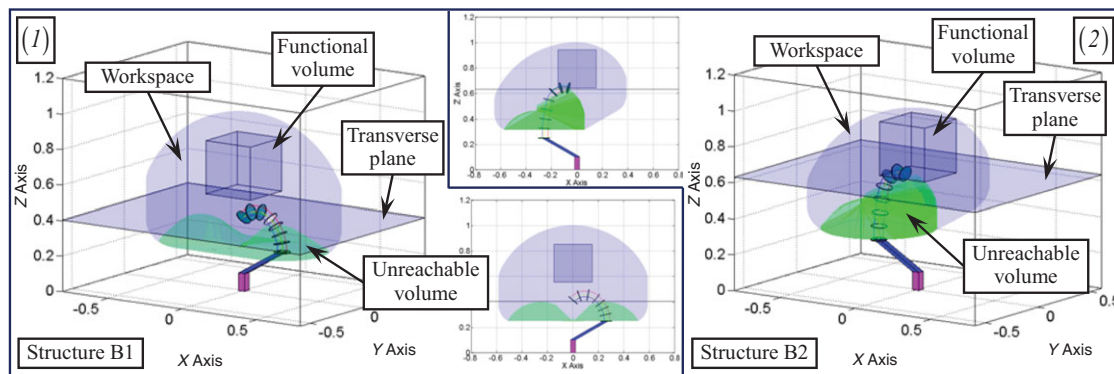Fig. 7. (Colour online) Routing of the segments' backbones forms addition constraints.

Fig. 8. (Colour online) Translational workspace of Structure B: (1) Structure B1 and (2) Structure B2 whose parameters are in Table II.

also be noted that this change of the optimization objective function cannot be generalized to other types of manipulators because of the specific kinematic characteristics of these continuum segments.

5.1. Kinematic optimization of Structure A
The configuration vector of Structure A is defined as $\boldsymbol{\xi}_A = [\, \phi \;\; \boldsymbol{\psi}_3^T \;\; \boldsymbol{\psi}_2^T \;\; \boldsymbol{\psi}_1^T \,]^T$. The structural design parameters include i, r, L_t, and δ_{ti} as in Table I. When the kinematic performance is to be optimized, the free variables only include L_t ($t = 1, 2, 3$). The other design parameters (i, r, and δ_{ti}) only affect
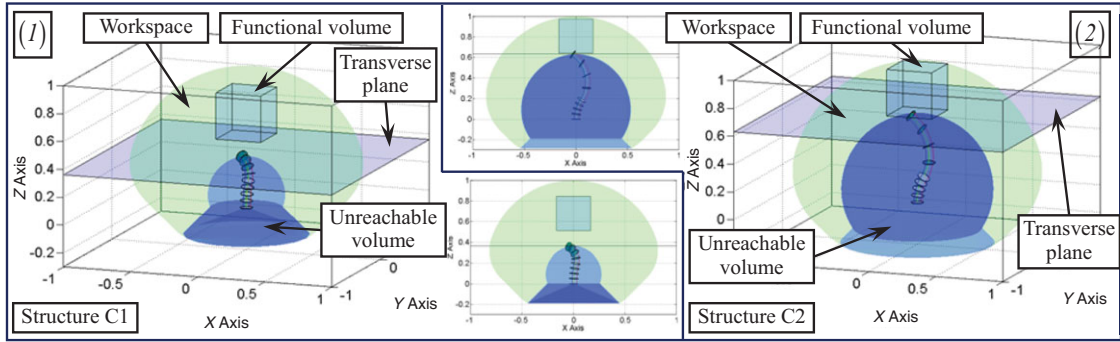
Fig. 9. (Colour online) Translational workspace of Structure C: (1) Structure C1 and (2) Structure C2.

the arrangement of the secondary backbones and the actuation; they could be determined by other design criteria, such as stiffness, actuation forces, etc.

The optimization of L_t $(t = 1, 2, 3)$ was conducted to maximize the margin between the functional volume and the boundary of the manipulators' translational workspace. Referring to Figs. 6–3, the cubic functional volume is relatively small compared to the translational workspace and the margin around it is quite big. The critical margin is the space above and below the functional volume. If a transverse plane could reach a lower point, the upper and the lower margins could be increased. The cost function of this optimization is hence defined as the lowest point a transverse plane can reach (the lowest top of the unreachable volume).

The total reach of Structure A is 1; namely, $L_1 + L_2 + L_3 = 1$. Results of this study can be easily scaled for an actual case. An example of the functional volume is a cube of 50 mm × 50 mm × 50 mm, which is required by a cholecystectomy.[9,44] According to the aforesaid ratio of the manipulator length over the cube edge length, this study assumes a cubic functional volume of $0.3 \times 0.3 \times 0.3$.

Optimization of L_t $(t = 1, 2, 3)$ is conducted in an enumerative manner. In Fig. 6–1, the lowest point which a transverse plane could reach is depicted with L_1 and L_2 varying from 0 to 1 in increments of 0.05. Since the optimization is performed by scanning the entire variable space, the translational workspace shall be evaluated repeatedly for all the possible combinations of L_t $(t = 1, 2, 3)$. As the evaluation of the workspace is a time-consuming process, an increment of 0.05 was used in order to finish the optimization within a reasonable amount of time, although a smaller increment would lead to a finer scanning for more accurate optimization results.

As shown in Fig. 6–1, the lowest reach was realized when $L_1 = 0.65$ and $L_2 = 0$, indicated by the point M1; the corresponding configuration of Structure A is plotted in Fig. 6–2. Clearly it is not possible to construct a continuum segment whose length is zero. In practical implementations, allowed elastic strain and diameters of the backbones will put a constraint on the minimal length of each segment. Here, additional constraints are introduced as below, with the understanding that these constraints could be modified in an actual case:

$$L_t \geq 0.2, \quad t = 1, 2, 3 \tag{27}$$

With the constraints as in Eq. (27), a triangular area is marked in Fig. 6–1, bounded by three lines ($L_1 = 0.2$, $L_2 = 0.2$, and $L_1 + L_2 = 0.8$). Within this area, a feasible optimum is indicated by the point M2 with a configuration of $L_1 = 0.35$, $L_2 = 0.20$, and $L_3 = 0.45$. This configuration is plotted in Figs. 6–3 and it will be used in the comparison presented in Section 6. The design parameters are also summarized in Table II together with those of Structure B and Structure C.

5.2. Kinematic optimization of Structure B
Referring to Fig. 4 and Section 4.3, design parameters of Structure B include $z_{\min}$, $z_{\max}$ (motion range of Link Z), h (translation of Linkage H in a direction specified by ς), i, r, δ_{ti}, L_1, and L_2. Among these design parameters, $z_{\min}$, $z_{\max}$, h, L_1, and L_2 affect the kinematics and they will be optimized.

A feasible optimal configuration of Structure A is obtained with respect to the constraints as in Eq. (27). This constraint has an equivalent form for its minimal bending radius ρ_t as in Eq. (28),

since the segment of length L_t undergoes a $\pi/2$ bending. Hence, Structure B shall be optimized with respect to the consistent constraint. Referring to Figs. 7 and 4, backbones of the continuum segments in Structure B are routed through a flexible multi-lumen tube to prevent them from buckling during actuation. Bending radius ρ of this tube shall be subject to the same constraint as in Eq. (28). When linkage H opens to its maximum at $\varsigma = 5\pi/6$ and Link Z lowers to its minimum at $z = z_{\min}$, the routing tube possesses a minimal bending radius. If the shape of the multi-lumen tube could be approximated by two circular arcs, constraints on h and $z_{\min}$ can be derived as in Eq. (29):

$$L_t \geq 0.2 \overset{\theta_{tL} \leq \pi/2}{\longleftrightarrow} \rho_t \geq 2/5\pi \,, t = 1, 2 \tag{28}$$

$$\left. \begin{array}{r} \rho \geq 2/5\pi \\ 2\rho = h \cos(\pi - \varsigma) \\ 2\rho = h \sin(\pi - \varsigma) + z_{\min} \end{array} \right\} \overset{\varsigma = \frac{5\pi}{6}}{\longrightarrow} \left\{ \begin{array}{l} h \geq \frac{8}{5\pi\sqrt{3}} \approx 0.294 \\ z_{\min} \geq \frac{4}{5\pi} \left(1 - \frac{1}{\sqrt{3}}\right) \approx 0.108. \end{array} \right. \tag{29}$$

Optimization of Structure B is formulated to minimize the lowest point that a transverse plane can reach. Constraints from Eqs. (28) to (29) are rounded as in Eq. (30)

$$z_{\max} > z_{\min} \geq 0.11, \quad h \geq 0.30, \quad L_1 \geq 0.20, \quad L_2 \geq 0.20$$
$$z_{\max} + h + L_1 + L_2 = 1. \tag{30}$$

The translation of Link Z tends to stay at $z_{\min} = 0.11$ when such a transverse plane reaches for a lower point. Then h, L_1 and L_2 vary, $z_{\max}$ can be obtained from $z_{\max} = 1 - h - L_1 - L_2$. The optimization is again conducted in an enumerative manner with the variables varying within the allowed ranges with increments of 0.05.

When the joint limit $\varsigma \in [\pi/6, 5\pi/6]$, the optimal configuration of Structure B is obtained: $L_1 = 0.2$, $L_2 = 0.2$, $h = 0.30$ and $z \in [0.11, 0.30]$. If the design parameters of the IREP robot's manipulator[9–11] is normalized with respect to the manipulator's length (gripper excluded), the actual configuration deviates from the optimal configuration. It might be beneficial to include the actual design in this comparison. Structure B under the optimal configuration is hence referred to as Structure B1, whereas the actual configuration is referred to as Structure B2. Design parameters of both Structure B1 and Structure B2 are summarized in Table II. The translational workspaces of both structures are plotted in Fig. 8. Besides the differences in the component lengths, the joint limits for ς are also different ($\varsigma \in [\pi/6, 5\pi/6]$ for Structure B1 and $\varsigma \in [\pi/2, 5\pi/6]$ for Structure B2). This is due to the difficulty in realizing such a more favorable actuation of the Linkage H in the IREP robot. A functional workspace of a cube of $0.3 \times 0.3 \times 0.3$ is fitted within the translational workspace in Fig. 8.

5.3. Kinematic optimization and dimension synthesis of Structure C

Referring to Fig. 5 and Section 4.4, design parameters of Structure C include $L_{1\_\min}$, $L_{1\_\max}$, $L_{2\_\min}$, and $L_{2\_\max}$, since the segment in Structure C can actively change its length.

The optimization of maximizing the margin between the cubic functional volume and the translational workspace is subject to the following constraints:

$$L_{1\_\min} \geq 0.2, \ L_{2\_\min} \geq 0.2 \quad \text{and} \quad L_{1\_\max} + L_{2\_\max} = 1. \tag{31}$$

The enumerative optimization gives the optimal configuration of Structure C as $L_1 \in [0.2, 0.5]$ and $L_2 \in [0.2, 0.5]$, which is plotted in Figs. 9–1 and listed in Table II as Structure C1. It was noted that in this configuration, $L_{t\_\max}$ is 2.5 times of $L_{t\_\min}$, which might be subject to difficulties in actual realization. In order to provide a lower bound of joint ranges of L_1 and L_2, a dimension synthesis is performed to match the lowest reach of the transverse plane of Structure C to that of Structure A. Multiple resolutions were found, such as $L_1 \in [0.2, 0.35]$ with $L_2 \in [0.5, 0.65]$, $L_1 \in [0.2, 0.4]$, with $L_2 \in [0.4, 0.6]$. The translational workspace of the configuration of $L_1 \in [0.2, 0.35]$ and $L_2 \in [0.5, 0.65]$ is plotted in Figs. 9–2 and summarized in Table II as Structure C2. Including Structure C2 in the comparison provide a compromise point between selecting Structure A or realizing the minimal

Table II. Design parameters of the structures to be compared.

| For all the segments $\boldsymbol{\psi}_t = [\theta_{tL} \delta_t]^T$		$\theta_{tL} \in [0, \pi/2]$	$\delta_t \in [-\pi, \pi]$
Structure A	Configuration vector $\boldsymbol{\xi}_A = \left[\phi \ \boldsymbol{\psi}_3^T \ \boldsymbol{\psi}_2^T \ \boldsymbol{\psi}_1^T \right]^T$		
$\phi \in [-\pi, \pi]$ $\quad L_1 = 0.35$		$L_2 = 0.20$	$L_3 = 0.45$
Structure B1	Configuration vector $\boldsymbol{\xi}_B = \left[\phi \ \boldsymbol{\psi}_2^T \ \boldsymbol{\psi}_1^T \ \varsigma \ z \right]^T$		
$\phi \in [-\pi, \pi]$ $\quad L_1 = 0.2$ $h = 0.30$ $\quad\quad \varsigma \in [\pi/6, 5\pi/6]$		$L_2 = 0.2$ $z \in [0.11, 0.30]$	
Structure B2	Configuration vector $\boldsymbol{\xi}_B = \left[\phi \ \boldsymbol{\psi}_2^T \ \boldsymbol{\psi}_1^T \ \varsigma \ z \right]^T$		
$\phi \in [-\pi, \pi]$ $\quad L_1 = 0.3$ $h = 0.30$ $\quad\quad \varsigma \in [\pi/2, 5\pi/6]$		$L_2 = 0.2$ $z \in [0.11, 0.20]$	
Structure C1	Configuration vector $\boldsymbol{\xi}_C = \left[\phi \ \boldsymbol{\psi}_2^T \ L_2 \ \boldsymbol{\psi}_1^T \ L_1 \right]^T$		
$\phi \in [-\pi, \pi]$ $\quad L_1 \in [0.2, 0.5]$		$L_2 \in [0.2, 0.5]$	
Structure C2	Configuration vector $\boldsymbol{\xi}_C = \left[\phi \ \boldsymbol{\psi}_2^T \ L_2 \ \boldsymbol{\psi}_1^T \ L_1 \right]^T$		
$\phi \in [-\pi, \pi]$ $\quad L_1 \in [0.2, 0.35]$		$L_2 \in [0.5, 0.65]$	
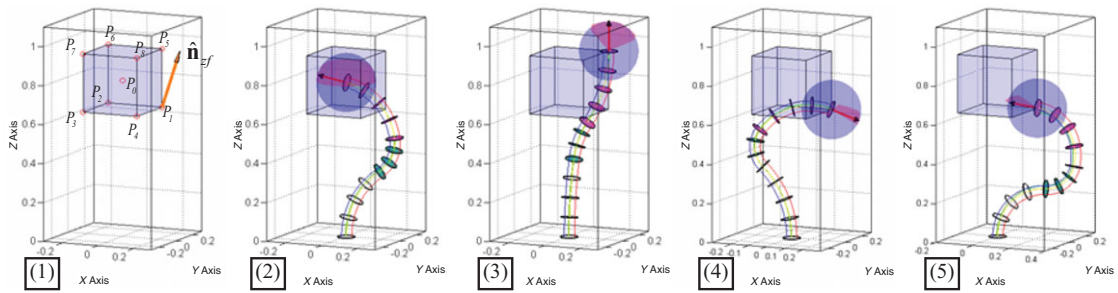
Fig. 10. (Colour online) Kinematic performance evaluated at selected points for Structure A: (1) annotation for all the selected points, (2) at P_0, (3) at P_5, (4) at P_1 pointing inward, and (5) at P_1 pointing outward.

joint ranges of Structure C. A functional workspace of $0.3 \times 0.3 \times 0.3$ is fitted in the translational workspace and plotted in Fig. 9.

The optimization results of Structure C2 also indicate the previous design practice following a designer's intuition might not be optimal. Structure C2 has a longer distal segment with a shorter proximal segment.

6. Comparison Results and Discussions
Kinematic performance of the three structures at selected points (the center and the vertices of a desired functional volume) is evaluated as a solid angle swept by the wrist's axis. Since the lowest reach of the transverse plane of a structure is different from one another, the functional volume is fitted in the middle of the translation workspace above the unreachable volume as in Figs. 6, 8, and 9. In this way, the margin above and below the functional volume is approximately evenly distributed. The annotation of the selected points shown in Figs. 10–1 is identical for all the structures. Please be noted that optimal placement of the functional volume within the translational workspace might be complicated particularly if not only translation but also rotation of the volume would be considered. In order to keep the current content coherent, the functional volume is placed in the middle even though the placement might favor one structure slightly over another.

The evaluation of the kinematic performance at each point involves the following four steps.

1. From an initial configuration, each structure was driven toward the selected point by only specifying the linear velocity and a kinematics redundancy resolution as in Eq. (32). A standard resolved rate control method[45] was used to drive the manipulators toward a desired position and/or an orientation in the simulations.
2. When the selected point is reached, each structure was driven to verify whether a direction could be aligned by the wrist's axis. The verification was implemented as follows:

(a) A unit direction vector $\hat{\mathbf{n}}_{zf}$ was first parameterized using two variables. A possible parameterization is shown in Eq. (33) and $\hat{\mathbf{n}}_{zf}$ is indicated in Fig. 10–1. An arbitrary unit vector $\hat{\mathbf{n}}_{xf}$ which is normal to $\hat{\mathbf{n}}_{zf}$ is then picked to form a desired orientation of the end effector. Because of the rotary wrist, $\hat{\mathbf{n}}_{xf}$ would not affect the reachability of $\hat{\mathbf{n}}_{zf}$.
(b) Each structure was driven by specifying a $\dot{\mathbf{x}}$ with a linear velocity preceding an angular velocity. The linear velocity always pointed towards the selected point. The angular velocity was generated from a rotation matrix from the current orientation to the desired one. The standard resolved rate control method was used to drive the manipulator. The singularity-robust inverse Jacobian was used during the process, as shown in Eq. (34).
(c) The direction of $\hat{\mathbf{n}}_{zf}$ is considered reachable when (i) the condition number $\kappa(\mathbf{J}_N) \leq 10^3$, (ii) the joint limits were not reached, (iii) the tip position error is smaller than 10^{-3}, and (iv) the orientation error is smaller than $3.5 \times 10^{-3} = 0.2°$.
3. The parameterization of $\hat{\mathbf{n}}_{zf}$ as in Eq. (33) varies φ_1 and φ_2 in increments of $2°$. The process repeats itself till the parameterization is fully tested.
4. The kinematic performance at this point is evaluated though a two-dimensional numerical integral following the definition of a solid angle.

$$\dot{\boldsymbol{\xi}}_N = (\mathbf{J}_{N\_\mathbf{v}})^+ \mathbf{v}, \tag{32}$$

where $N = A$, B or C, $\mathbf{J}_{N\_\mathbf{v}}$ is the linear velocity portion of $\mathbf{J}_N$ as in Eqs. (9), (15), and (23) and $\mathbf{v}$ is the linear velocity pointing toward the selected point.

$$\hat{\mathbf{n}}_{zf} = [\sin\varphi_1\cos\varphi_2 \quad \sin\varphi_1\sin\varphi_2 \quad \cos\varphi_1]^T, \quad \varphi_1 \in [0, \pi] \quad \text{and} \quad \varphi_2 \in [0, 2\pi], \tag{33}$$

$$\dot{\boldsymbol{\xi}}_N = \begin{cases} \mathbf{J}_N^T (\mathbf{J}_N\mathbf{J}_N^T)^{-1} \dot{\mathbf{x}}, & \text{when } \kappa(\mathbf{J}_N) \leq 10^3 \\ \mathbf{J}_N^T (\mathbf{J}_N\mathbf{J}_N^T + \lambda\mathbf{I})^{-1} \dot{\mathbf{x}}, & \text{when } \kappa(\mathbf{J}_N) > 10^3 \end{cases} \tag{34}$$

where $N = A$, B or C, $\mathbf{J}_N$ is as in Eqs. (9), (15) and (23), and $\kappa(\mathbf{J}_N)$ is the condition number of $\mathbf{J}_N$.

Verifying whether an orientation at a selected point is reachable is essentially verifying whether an inverse kinematics problem has a solution. Without an analytical solution, the resolved rate method is just like solving the inverse kinematics problem numerically. The initial configuration also affects whether the process converges to a solution. The aforementioned four-step process might have to be repeated from randomly generated initial configurations repeatedly in order to make sure the results are conclusive. Actually this is also how disconnected patches as in Figs. 10–4 and 10–5 are discovered.

The values of the evaluated kinematic performances of the three structures are presented in Table III. Due to the structural symmetry, some values should be identical: (i) those at the P_1 to P_4 points of Structure A, Structure C1 and C2; (ii) those at the P_5 to P_8 points of Structure A, Structure C1 and C2; (iii) those at the P_1 and P_4 points, those at the P_2 and P_3 points, those at the P_6 and P_7 points and those at the P_5 and P_8 points of Structure B1 and Structure B2. The evaluated values are slightly different due to computation accuracy.

The evaluated kinematic performance can be visualized as a patch on the surface of a sphere as in Figs. 10–12. The attached multimedia extension shows simulations where the wrist's axis of each structure swept boundaries of these patches.

Table III. Kinematic performance of the structures (unit: steradian).

|				
Structure A	P_1: 0.623	P_2: 0.601	P_3: 0.614	P_4: 0.634
P_0: 4.467	P_5: 1.397	P_6: 1.412	P_7: 1.428	P_8: 1.391
Structure B1	P_1: 1.644	P_2: 1.902	P_3: 1.904	P_4: 1.642
P_0: 7.456	P_5: 1.886	P_6: 2.134	P_7: 2.133	P_8: 1.886
Structure B2	P_1: 1.407	P_2: 1.470	P_3: 1.483	P_4: 1.395
P_0: 2.023	P_5: 0.842	P_6: 0.842	P_7: 0.829	P_8: 0.831
Structure C1	P_1: 2.739	P_2: 2.712	P_3: 2.698	P_4: 2.735
P_0: 4.031	P_5: 2.616	P_6: 2.561	P_7: 2.589	P_8: 2.609
Structure C2	P_1: 0.738	P_2: 0.712	P_3: 0.705	P_4: 0.723
P_0: 3.267	P_5: 0.519	P_6: 0.491	P_7: 0.503	P_8: 0.526
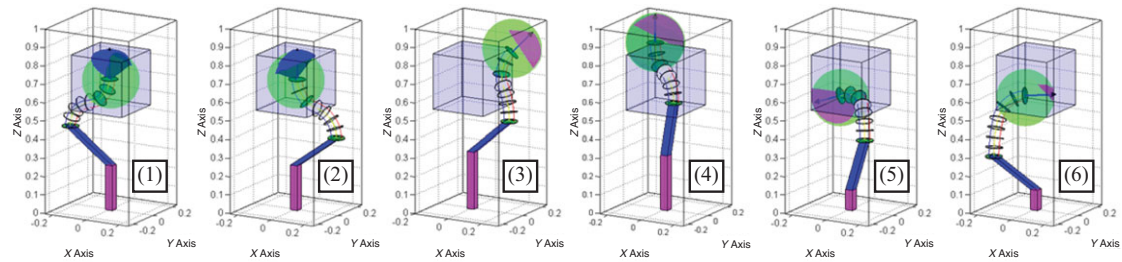
Fig. 11. (Colour online) Kinematic performance evaluated at selected points for Structure B1: (1)(2) at P_0, (3) at P_5, (4) at P_6, and (5)(6) at P_2; the kinematic performance of Structure B2 can be qualitatively visualized by insets (2) $\sim$ (5) where the Linkage H only opens to one side.
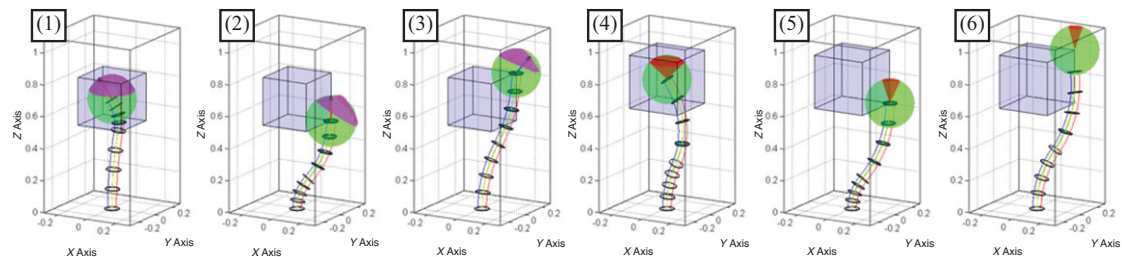

Fig. 12. (Colour online) Kinematic performance evaluated at selected points for Structure C1 and C2: (1)(4) at P_0, (2)(5) at P_1, and (3)(6) at P_5.

Please note that in Figs. 10–4 and 10–5 there are two disconnected patches at P_1; the same characteristic is also shown in Figs. 11–5 and 11–6. These two disconnected patches can only be reached by driving the tip of the manipulator away from and then back to the selected point. Although the two patches overlap in Figs. 11–1 and 11–2, the combined patch cannot be fully reached without moving the manipulator tip away from and then back to the P_0 point in order to open the Linkage H to the other side. The kinematic performance of Structure B2 can be qualitatively visualized as in Figs. 11–2 to 11–5 where the Linkage H only opens to one side.

From the values presented in Table III, Structure A had an average of 1.396 for the evaluated kinematic performance, whereas Structure B1 has an average of 2.510, Structure B2 has an average of 1.236, Structure C1 has an average of 2.810 and Structure C2 has an average of 0.909. Before a conclusion can be reached which structure is more desired, some insights can be observed as follows.

- The performance of Structure C1 at points through P_1 to P_8 is considerably higher than that of Structure C2. This is because these points are substantially further away from the boundaries of the translational workspaces, referring to Fig. 9. The results echo the optimization approach in Section 5 that maximizing the margins between the vertices and the boundaries will lead to a better kinematic performance.
- The kinematic performance of Structure A at P_0, indicated by the red patch in Figs. 10–2, excludes the top portion. Although the numerical value is quite big, it is less desired since the manipulator can

Table IV. A summary of the comparison characteristics.

General characteristics	Maximizing the margins between the vertices and the workspace boundary will lead to a better kinematic performance. This is because points on the boundary of the translational workspace usually involve its segments in straight or maximally bent shapes. Zero or maximal bending reduces the orientation capability.
Structure A	The structure has acceptable evaluation values but the quality might not be good enough. This results from the constant lengths of the three segments. The manipulator bends its segments to reach a position as well orient a surgical tool. Pinpointing a point limits its orientation range.
Structure B	The Link Z and Linkage H help improve the dexterity because the structure now does not solely depend on the bending of the segments to reach a point.
Structure C	Structure C1 has the highest dexterity because the segments vary its lengths to sweep the functional volume and bend more or less to orient surgical tools. When an implementation is challenging, Structure C2 provides a reference point where a designer could start considering Structure A or B over C.

only orient a surgical tool sideward. A more desired performance is like that at P_5 as in Figs. 10–3, where the manipulator can orient tools upward and sideward. A worse performance is at P_1 where the performance has two disconnected parts as in Figs. 10–4 and 10–5. These two insets can be viewed as two manipulators were inserted to perform a task cooperatively at P_1. Their capabilities are really limited due to the small orientation ranges. The performances at P_2 to P_4 should be theoretically identical to that at P_1 due to the structural symmetry. The performance characteristics of Structure A result from the constant lengths of the three segments. The manipulator bends its segments to reach a position as well as orient a surgical tool. Pinpointing a point limits its orientation range.

- The performance of Structure B1 at P_0 has two overlapping but essentially disconnected parts as mentioned previously. At P_1 to P_4, performances of Structure B1 and Structure B2 are better than those of Structure A because the Link Z (please refer to Fig. 7) can be lowered and the structure does not solely depend on the bending of the segments to reach a lower point. Figs. 11–5 and 11–6 can be again viewed as two inserted manipulators to perform a task cooperatively at P_2. Now the situation is slightly better than that of Structure A since at least one manipulator as in Fig. 11–5 could help more.

- From Table III, the performances of Structure B2 seem a lot worse than those of Structure B1. This is because the performance of Structure B1 at each point usually include two parts when the Linkage H (please refer to Fig. 7) opens to both sides. But it is acceptable that the Linkage H only opens to one side as in the IREP manipulator,[9–11] since in a dual-arm operation a desired orientation can always be reached by one or the other manipulator. Performances of Structure B2 at P_5 to P_8 are less than the half of those of Structure B1 because the component dimensions in Structure B2 were not optimized.

- Performance evaluations of Structure C1 are substantially higher than those of the others and the performances are also of better quality. The essential reason is that the segments vary its lengths to sweep the functional volume and bend more or less to orient surgical tools. This structure is highly desired for actual surgical tasks. For example, if a manipulator needs to pull a tissue from P_5 to P_1 without flipping its tip's orientation, Structure C would be the only capable candidate. Since Structure C1 might be subject to difficulties in its realization, Structure C2 acts as a reference structure whose performance is closer to those of Structure A and Structure B but the length variation ranges are smaller than those of Structure C1. Depending on whether a desired length variation could be realized, a designer could make a more confident choice between Structure C and Structure A or Structure B. To be noted, the performance of Structure C2 at P_0 improves from those at P_1 to P_8. If the functional volume is smaller, Structure C2 could still be a better choice.

These observations are also summarized in Table IV.

7. Conclusions

This paper presented a comparison for kinematic performances among three different continuum manipulators which could all be potentially applied in one-port-access robotic surgeries, such as robotic SPA surgeries and robotic NOTES procedures. The three structures were firstly optimized so as to ensure a more fair and consistent comparison. The optimization results indicate the previous design practice following a designer's intuition might not be optimal. For instance, the Structure C should be designed to have a longer distal segment with a shorter proximal segment.

In total, five derivative structures were eventually compared and the comparison results were discussed. The best kinematic performance belongs to Structure C1, which consists of two 3-DoF continuum segments with relatively large variation ranges of its segment lengths. Such a structure would not only generate a bigger workspace but also allow surgeons to orient tools more freely. If the variation ranges of the segment lengths are reduced, the kinematic performance of Structure C deteriorates. When the ranges match those of Structure C2, the kinematic performance becomes comparable to those of Structure A and Structure B; the translational workspace of Structure C2 also barely envelops the desired functional volume.

The optimizations and comparison were conducted in a dimensionless manner and they can be easily scaled for a practical case. The results could serve as a design reference for future development of one-port-access surgical robots. Quantitative guidelines include the following two aspects. Firstly if a length varying range larger than that of Structure C2 can be actually materialized, Structure C should be adopted for better kinematic performance. Secondly, in order to envelop a specific functional volume, manipulator designs using Structure A, B or C can refer to Table II, Figs. 6, 8, and 9 proportionally so that the translational workspace could be big enough.

Even when more complicated structures are to be designed using such continuum segments, inspirations can be extracted from the results and two qualitative guidelines for better kinematic performance can be considered. Firstly, a component or a mechanism for translation and/or length variation should be incorporated so that bending of the segments contributes more to orienting surgical tools. What is more, it is counterintuitive to know that a distal segment should be longer than or at least equal to a proximal segment (referring to Structure A and C as in Table II) to produce better kinematic performance. Many existing designs possess shorter distal segments and longer proximal segments.

Results of this paper are not limited to the designs using multi-backbone continuum segments as in Fig. 3. They could be applied to a variety of different designs as long as the design consists of continuum segments whose curvatures remain constant.

This paper concerns kinematic performances of the three different continuum manipulators. Once parameters for kinematics are determined, other parameters (e.g., sizes and arrangements of secondary backbones) could be considered for more desired mechanical properties, such as payload, controllable stiffness, etc.

References
1. R. D. Howe and Y. Matsuoka, "Robotics for surgery," *Annu. Rev. Biomed. Eng.* **1**, 211–420 (1999).
2. P. Dario, B. Hannaford and A. Menciassi, "Smart surgical tools and augmenting devices," *IEEE Trans. Robot. Autom.* **19**(5), 782–792 (2003).
3. R. H. Taylor, "A Perspective on Medical Robotics," *Proc. IEEE* **94**(9), 1652–1664 (2006).
4. D. Pisla, B. Gherman, C. Vaida and N. Plitea, "Kinematic modelling of a 5-DOF hybrid parallel robot for laparoscopic surgery," *Robotica* **30**(07), 1095–1107 (2012).
5. D. Pisla, B. Gherman, C. Vaida, M. Suciu and N. Plitea, "An active hybrid parallel robot for minimally invasive surgery," *Robot. Comput. Integr. Manuf.* **29**(4), 203–221 (2013).
6. G. Navarra, E. Pozza, S. Occhionorelli, P. Carcoforo and I. Donini, "One-wound laparoscopic cholecystectomy," *Br. J. Surg.* **84**(5), 695 (1997).

7. S. A. Giday, S. V. Kantsevoy and A. N. Kalloo, "Principle and History of Natural Orifice Translumenal Endoscopic Surgery (NOTES)," *Minimally Invasive Ther. Allied Technol.* **15**(6), 373–377 (2006).

8. P. Plinkert and H. Lowenheim, "Trends and perspectives in minimally invasive surgery in otorhinolaryngology-head and neck surgery," *Laryngoscope* **107**, 1483–1489 (1997).

9. K. Xu, R. E. Goldman, J. Ding, P. K. Allen, D. L. Fowler and N. Simaan, "System Design of an Insertable Robotic Effector Platform for Single Port Access (SPA) Surgery," *Proceedings of the IEEE/RSJ International Conference on Intelligent Robots and Systems (IROS)*, St. Louis, MO, USA (2009) pp. 5546–5552.

10. J. Ding, K. Xu, R. Goldman, P. K. Allen, D. L. Fowler and N. Simaan, "Design, Simulation and Evaluation of Kinematic Alternatives for Insertable Robotic Effectors Platforms in Single Port Access Surgery," *Proceedings of the IEEE International Conference on Robotics and Automation (ICRA)*, Anchorage, Alaska, USA (2010) pp. 1053–1058.

11. J. Ding, R. E. Goldman, K. Xu, P. K. Allen, D. L. Fowler and N. Simaan, "Design and coordination kinematics of an insertable robotic effectors platform for single-port access surgery," *IEEE/ASME Trans. Mechatronics* **18**(5), 1612–1624 (2013).

12. M. Piccigallo, U. Scarfogliero, C. Quaglia, G. Petroni, P. Valdastri, A. Menciassi and P. Dario, "Design of a novel bimanual robotic system for single-port laparoscopy," *IEEE/ASME Trans. Mechatronics* **15**(6), 871–878 (2010).

13. Y. Sekiguchi, Y. Kobayashi, Y. Tomono, H. Watanabe, K. Toyoda, K. Konishi, M. Tomikawa, S. Ieiri, K. Tanoue, M. Hashizume and M. G. Fujie, "Development of a Tool Manipulator Driven by a Flexible Shaft for Single Port Endoscopic Surgery," *Proceedings of the IEEE / RAS-EMBS International Conference on Biomedical Robotics and Biomechatronics (BIOROB)*, Tokyo, Japan (2010) pp. 120–125.

14. H. Lee, Y. Choi and B.-J. Yi, "Stackable 4-BAR manipulators for single port access surgery," *IEEE/ASME Trans. Mechatronics* **17**(1), 157–166 (2012).

15. M. Simi, M. Silvestri, C. Cavallotti, M. Vatteroni, P. Valdastri, A. Menciassi and P. Dario, "Magnetically activated stereoscopic vision system for laparoendoscopic single-site surgery," *IEEE/ASME Trans. Mechatronics* **18**(3), 1140–1151 (2013).

16. A. Degani, H. Choset, A. Wolf and M. A. Zenati, "Highly Articulated Robotic Probe for Minimally Invasive Surgery," *Proceedings of the IEEE International Conference on Robotics and Automation (ICRA)*, Orlando, Florida (2006) pp. 4167–4172.

17. D. J. Abbott, C. Becke, R. I. Rothstein and W. J. Peine, "Design of an Endoluminal NOTES Robotic System," *Proceedings of the IEEE/RSJ International Conference on Intelligent Robots and Systems (IROS)*, San Diego, CA, USA (2007) pp. 410–416.

18. A. C. Lehman, J. Dumpert, N. A. Wood, L. Redden, A. Q. Visty, S. Farritor, B. Varnell and D. Oleynikov, "Natural orifice cholecystectomy using a miniature robot," *Surgical Endoscopy* **23**(2), 260–266 (2009).

19. K. Harada, E. Susilo, A. Menciassi and P. Dario, "Wireless Reconfigurable Modules for Robotic Endoluminal Surgery," *Proceedings of the IEEE International Conference on Robotics and Automation (ICRA)*, Kobe, Japan (2009) pp. 2699–2704.

20. K. Xu, J. Zhao, J. Geiger, A. J. Shih and M. Zheng, "Design of an Endoscopic Stitching Device for Surgical Obesity Treatment Using a NOTES Approach," *Proceedings of the IEEE/RSJ International Conference on Intelligent Robots and Systems (IROS)*, San Francisco, CA, USA (2011) pp. 961–966.

21. J. Zhao, X. Zheng, M. Zheng, A. J. Shih and K. Xu, "An Endoscopic Continuum Testbed for Finalizing System Characteristics of a Surgical Robot for NOTES Procedures," *Proceedings of the IEEE/ASME International Conference on Advanced Intelligent Mechatronics (AIM)*, Wollongong, Australia (2013) pp. 63–70.

22. N. Simaan, K. Xu, A. Kapoor, W. Wei, P. Kazanzides, P. Flint and R. H. Taylor, "Design and integration of a telerobotic system for minimally invasive surgery of the throat," *Int. J. Robot. Res.* **28**(9), 1134–1153 (2009).

23. K. Xu and X. Zheng, "Configuration Comparison for Surgical Robotic Systems Using a Single Access Port and Continuum Mechanisms," *Proceedings of the IEEE International Conference on Robotics and Automation (ICRA)*, Saint Paul, MN, USA (2012) pp. 3367–3374.

24. K. Xu and N. Simaan, "Intrinsic wrench estimation and its performance index of multi-segment continuum robots," *IEEE Trans. Robot.* **26**(3), 555–561 (2010).

25. S. Hirose, *Biologically Inspired Robots, Snake-Like Locomotors and Manipulators* (Oxford University Press, Oxford, 1993).

26. I. A. Gravagne and I. D. Walker, "Uniform Regulation of a Multi-Section Continuum Manipulator," *IEEE International Conference on Robotics and Automation (ICRA)*, Washington, DC, USA (2002) pp. 1519–1524.

27. D. B. Camarillo, C. R. Carlson and J. K. Salisbury, "Configuration tracking for continuum manipulators with coupled tendon drive," *IEEE Trans. Robot.* **25**(4), 798–808 (2009).

28. C. Vaida, N. Plitea, D. Pisla and B. Gherman, "Orientation module for surgical instruments — A systematical approach," *Meccanica* **48**(1), 145–158 (2013).

29. T. Yoshikawa, "Manipulability of robotic mechanisms," *Int. J. Robot. Res.* **4**(2), 3–9 (1985).

30. C. A. Klein and B. E. Blaho, "Dexterity measures for the design and control of kinematically redundant manipulators," *Int. J. Robot. Res.* **6**(2), 72–83 (1987).

31. J. Angeles and C. S. López-Cajún, "Kinematic isotropy and the conditioning index of serial robotic manipulators," *Int. J. Robot. Res.* **11**(6), 560–571 (1992).
32. J. P. Merlet, "Determination of the orientation workspace of parallel manipulators," *J. Intell. Robot. Syst.* **13**, 143–160 (1995).
33. G. Carbone, E. Ottaviano and M. Ceccarelli, "An Optimum Design Procedure for Both Serial and Parallel Manipulators," *Proceedings of the Institution of Mechanical Engineers, Part C: Journal of Mechanical Engineering Science* **221**(7), 829–843 (2007).
34. K. Xu and N. Simaan, "An investigation of the intrinsic force sensing capabilities of continuum robots," *IEEE Trans. Robot.* **24**(3), 576–587 (2008).
35. B. A. Jones and I. D. Walker, "Kinematics for multisection continuum robots," *IEEE Trans. Robot. Autom.* **22**(1), 43–55 (2006).
36. R. J. Webster and B. A. Jones, "Design and kinematic modeling of constant curvature continuum robots: A review," *Int. J. Robot. Res.* **29**(13), 1661–1683 (2010).
37. G. S. Chirikjian and J. W. Burdick, "A modal approach to hyper-redundant manipulator kinematics," *IEEE Trans. Robot. Autom.* **10**(3), 343–354 (1994).
38. G. S. Chirikjian and J. W. Burdick, "Kinematically optimal hyper-redundant manipulator configurations," *IEEE Trans. Robot. Autom.* **11**(6), 794–806 (1995).
39. K. Zanganeh and J. Angeles, "The Inverse Kinematics of Hyper-Redundant Manipulators Using Splines," *IEEE International Conference on Robotics and Automation (ICRA)*, Nagoya, Japan (1995) pp. 2797–2802.
40. K. Xu and N. Simaan, "Analytic formulation for the kinematics, statics and shape restoration of multibackbone continuum robots via elliptic Integrals," *J. Mech. Robot.* **2**, (2010).
41. V. K. Chitrakaran, A. Behal, D. M. Dawson and I. D. Walker, "Setpoint Regulation of Continuum Robots Using a Fixed Camera," *American Control Conference*, Boston, Massachusetts, USA (2004) pp. 1504–1509.
42. D. C. Rucker and R. J. Webster, "Statics and dynamics of continuum robots with general tendon routing and external loading," *IEEE Trans. Robot* **27**(6), 1033–1044 (2011).
43. O. Bohigas, M. Manubens and L. Ros, "A complete method for workspace boundary determination on general structure manipulators," *IEEE Trans. Robot.* **28**(5), 993–1006 (2012).
44. E. Berber, K. L. Engle, A. Garland, A. String, A. Foroutani, J. M. Pearl and A. E. Siperstein, "A Critical analysis of intraoperative time utilization in laparoscopic cholecystectomy," *Surgical Endoscopy* **15**(2), 161–165 (2004).
45. D. E. Whitney, "Resolved motion rate control of manipulators and human prostheses," *IEEE Trans. Man-Mach. Syst.* **10**(2), 47–53 (1969).